Retrievals of nighttime electron density from Thermosphere Ionosphere Mesosphere Energetics and Dynamics (TIMED) mission Global Ultraviolet Imager (GUVI) measurements

R. DeMajistre, L. J. Paxton, D. Morrison and J.-H. Yee
Applied Physics Laboratory, The Johns Hopkins University, Laurel, Maryland, USA

L. P. Goncharenko
Haystack Observatory, Massachusetts Institute of Technology, Westford, Massachusetts, USA

A. B. Christensen
The Aerospace Corporation, Los Angeles, California, USA

Received 17 October 2003; revised 27 February 2004; accepted 15 March 2004; published 18 May 2004.

[1] In this work we will present a method for retrieving nighttime electron density profiles from OI 135.6 nm limb emissions measured by the Global Ultraviolet Imager (GUVI) aboard the Thermosphere Ionosphere Mesosphere Energetics and Dynamics (TIMED) mission spacecraft. The primary mechanism for 135.6 nm radiance in the nighttime thermosphere is recombination of O^+ ions, and the volume emission rate is approximately proportional to the square of the electron density. Herein we describe a two-step inversion method in which we first determine the volume emission rate as a function of altitude from the radiance measurements and then use the inferred volume emission rates to determine the electron density profile. There are two important factors that we have addressed in constructing the retrieval algorithms for this problem. First, the GUVI instrument was primarily designed for day side measurements. Consequently, the signal levels on the night side are very low, and our retrieval algorithms must therefore be able to function in regions where the signals are weak. Second, since we must take the square root of the volume emission rate, it must be everywhere positive in order for the electron density to be deduced. For this reason, we have imposed nonnegativity constraints (using the methods described by *Menke* [1989]) on what might otherwise be discrete linear retrievals of volume emission rate. After describing the retrieval method we present an error analysis and a preliminary comparison with coincident measurements by incoherent scatter radars (ISRs). In general, the retrieved electron densities from the GUVI data agree well with the ISR data, although more coincident measurements would increase our confidence in the resulting electron density profiles. *INDEX TERMS:* 2494 Ionosphere: Instruments and techniques; 2443 Ionosphere: Midlatitude ionosphere; 2415 Ionosphere: Equatorial ionosphere; 2467 Ionosphere: Plasma temperature and density; 2419 Ionosphere: Ion chemistry and composition (0335); *KEYWORDS:* electron density, TIMED/GUVI, inversion, low-latitude ionosphere

Citation: DeMajistre, R., L. J. Paxton, D. Morrison, J.-H. Yee, L. P. Goncharenko, and A. B. Christensen (2004), Retrievals of nighttime electron density from Thermosphere Ionosphere Mesosphere Energetics and Dynamics (TIMED) mission Global Ultraviolet Imager (GUVI) measurements, *J. Geophys. Res.*, *109*, A05305, doi:10.1029/2003JA010296.

1. Introduction

[2] Measurements of the Earth's ionosphere have been conducted over the years using a variety of remote and in situ measurements, from both ground-based and orbiting platforms. The different techniques and vantage points have provided us with a rich, though uneven, characterization of the ionosphere.

[3] Passive remote sensing methods use the naturally occurring emission from photochemical sources in the ionosphere as a means of remote sensing. The radiation mechanisms necessary for remote sensing are well understood and have been reviewed by *Meier* [1991]. Successful validated measurements of the nighttime ionosphere have been made using these methods [see, e.g., *Dymond et al.*, 2001]. A systematic study of the nighttime F region, however, has not been conducted using these techniques. In this work, we describe passive remote sensing techniques

0148-0227/04/2003JA010296$09.00

that are being used to infer the electron density in the nighttime F region with the Global Ultraviolet Imager (GUVI) instrument [*Christensen et al.*, 1994; *Paxton et al.*, 1999; L. J. Paxton et al., Global Ultraviolet Imager: Instrument description, calibration, and on-orbit performance, submitted to *Journal of Geophysical Research*, 2004] aboard the Thermosphere Ionosphere Mesosphere Energetics and Dynamics (TIMED) mission spacecraft. The GUVI measurement geometry and the TIMED orbit allow us to study the vertical, geographic, seasonal and local time dependence of the electron density.

[4] In this work we will present a method for retrieving electron density profiles from OI 135.6 nm limb emissions measured by TIMED/GUVI. There are two important factors that we have addressed in constructing the retrieval algorithms for this problem. First, the GUVI instrument was primarily designed for day side measurements as this is a TIMED mission priority. Consequently, the signal levels on the night side are very low. Our retrieval algorithms must therefore be able to function in regions where there may be only a few counts per 32 ms integration in the brightest areas of a given radiance profile. Clearly, information from multiple radiance profiles must be combined to achieve acceptable results. We, therefore, have taken care to combine these measurements correctly while doing our best to maintain a reasonable amount of spatial resolution. The second complicating factor relates to the photochemistry that gives rise to the measured radiance. In short, the electron density is approximately proportional to the square root of the 135.6 nm volume emission rate. Thus the volume emission rates that we infer from the measurements must be positive in order for the electron density to be deduced. For this reason, we have imposed nonnegativity constraints (using the methods described by *Menke* [1989]) on what might otherwise be discrete linear retrievals of volume emission rate.

[5] We will first describe the photochemistry that gives rise to the measured emissions. Next, the details of the GUVI measurements will be discussed. The method of inferring electron density profiles from the GUVI radiance measurements will then be presented. An error analysis of this technique will then be given. Finally, we will compare the EDPs inferred from the GUVI measurements with various ground-based data sets.

2. Emission Photochemistry

[6] Our technique employs measurements of 135.6 nm emission reported by GUVI. Before discussing the details of the GUVI measurement, we will describe the photochemical processes that give rise to this emission. This description will serve as a basis for the retrieval algorithms discussed in subsequent sections.

[7] The 135.6 nm emission is caused by relaxation of electronically excited atomic oxygen in the O(^5S) state to the ground O(^{3}P) state (see *Meier* [1991] for a full discussion). The volume emission rate is written as

$$\eta_{135.6} = A_1 \left[\mathrm{O}\left(^5S\right)\right], \tag{1}$$

where [O(^5S)] is the number density of O(^5S) and A_1 is the rate of the relaxation reaction. The lifetime of O(^5S) is sufficiently short ($\ll$1 s) that its concentration can be determined by the local photochemistry. The reactions that determine the O(^5S) concentration in the nighttime low-latitude thermosphere are given in Table 1.

Table 1. Relevant Photochemical Reactions[a]

Reaction	Rate	Reference
$O^+ + e \rightarrow O(^5S)$	$R_1 = 7.3 \times 10^{-13}$[b]	*Meléndez-Alvira et al.* [1999]
$O^- + O^+ \rightarrow O(^5S) + O$	$R_2 = 10^{-7}$[b]	*Olson et al.* [1971]
$O + e \rightarrow O^- + h\nu$	$R_3 = 1.3 \times 10^{-15}$[b]	*Massey* [1969]
$O^- + O \rightarrow O_2 + e$	$R_4 = 1.4 \times 10^{-10}$[b]	*Fehsenfeld et al.* [1969]
$O(^5S) \rightarrow O + h\nu$	$A_1 = 5.8 \times 10^{3}$[c]	*Zeippen et al.* [1977]
$O^+ + O_2 \rightarrow O_2^+ + O$	$R_5 = 1.2 \times 10^{-11}$[b]	*Roble et al.* [1987][d]
$O^+ + N_2 \rightarrow NO^+ + O$	$R_6 = 5.3 \times 10^{-13}$[b]	*Roble et al.* [1987][d]
$O_2^+ + e \rightarrow 2O$	$R_7 = 1.0 \times 10^{-7}$[b]	*Roble et al.* [1987][d]
$NO^+ + e \rightarrow N + O$	$R_8 = 1.3 \times 10^{-7}$[b]	*Roble et al.* [1987][d]

[a]The electron, ion, and neutral temperatures for the reaction rates given in the table are assumed to be 1160°K. Photochemical calculations in the body of this work use explicit temperature dependencies given in the references.
[b]In cm^3 s^{-1}.
[c]In s^{-1}.
[d]See Table 2 of this reference for temperature dependence and original references.

[8] From Table 1 we see that there are essentially three processes that determine the O(^5S) concentration. First, the reaction governed by R_1 is the recombination of atomic oxygen ions which serves as the direct source of O(^5S). Next, the reactions governed by R_2, R_3 and R_4 comprise the processes of attachment and mutual neutralization. Electrons attach themselves through R_3 to oxygen atoms yielding negatively charged oxygen ions. The oppositely charged atomic oxygen ions can form a neutral pair of atoms through R_2, one of which is in the O(^5S) state. The reaction R_4 competes with R_2 as a loss mechanism of negatively charged ions. Finally, the reaction governed by A_1, radiative relaxation, is the loss process that balances the above production mechanisms. Under the assumption of photochemical equilibrium, the concentration of O(^5S) can be written as

$$\left[\mathrm{O}\left(^5S\right)\right] = \frac{[\mathrm{O}^+][e]R_1}{A_1}(1 + \epsilon_{mn}), \tag{2}$$

where the quantities involved in mutual neutralization are contained in

$$\epsilon_{mn} \equiv \frac{R_3/R_1}{[\mathrm{O}^+]/[\mathrm{O}] + R_4/R_2}. \tag{3}$$

[9] Figure 1 shows typical numerical values of ϵ_{mn} as a function of altitude and local time. The contribution of mutual neutralization is slightly more than 10% at 100 km and drops off very quickly above 200 km. Figure 2 shows the altitude at which ϵ_{mn} is 0.02, along with the altitude of the electron density peak. From this figure we see that mutual neutralization only becomes a factor below 250 km. Further, almost everywhere the contribution becomes significant at altitudes at least 100 km below the electron density peak. For these reasons we are justified in ignoring the contribution of mutual neutralization in our subsequent calculations.

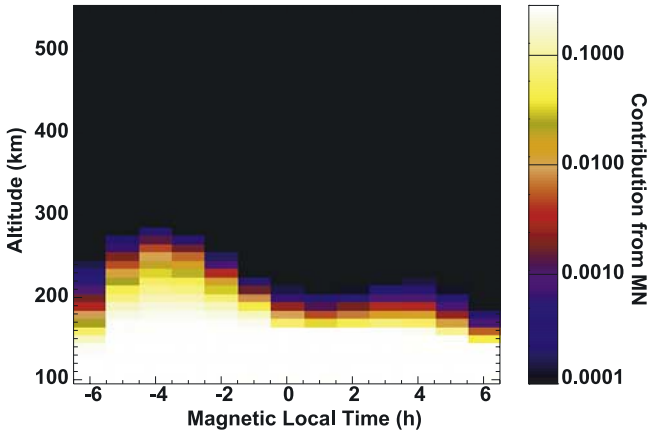

Figure 1. Contribution from mutual neutralization, ϵ_{mn} (see equation (3)), to the O(^5S) concentration as a function of altitude and magnetic local time. In the calculations of this contribution, [O] profiles were taken from MS90E [*Hedin*, 1991] and [O^+] profiles were taken from IRI 2000 [*Bilitza*, 2001]. The quantities were calculated at the equator near equinox.

[10] Combining equations (1) and (2) and neglecting the mutual neutralization contributions allows us to write the volume emission rate in the form

$$\eta_{135.6} = [O^+][e]R_1. \tag{4}$$

If we assume that the ionosphere is electrically neutral, then the sum of the ion densities should be equal to the electron densities. For the altitude region of interest, this implies

$$[e] = [O^+] + [O_2^+] + [NO^+] + [H^+]. \tag{5}$$

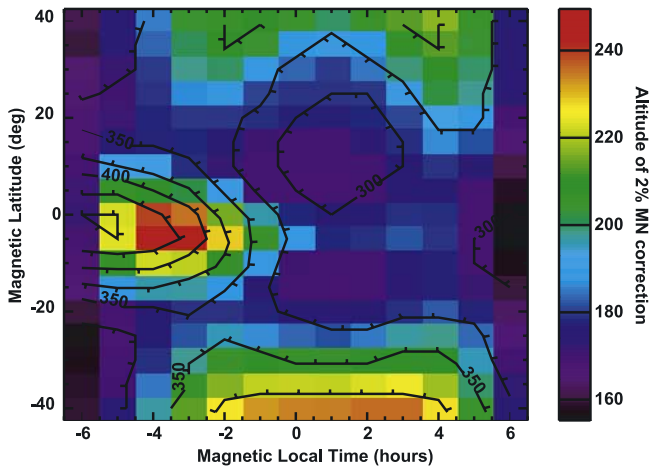

Figure 2. Altitude where the mutual neutralization term, ϵ_{mn} (see equation (3)), is equal to 0.02 as a function of altitude and magnetic local time. The labeled contours (with marks indicating decreasing values) show the altitude of the peak electron density given by International Reference Ionosphere (IRI) 2000 [*Bilitza*, 2001] at the given latitude and magnetic local time.

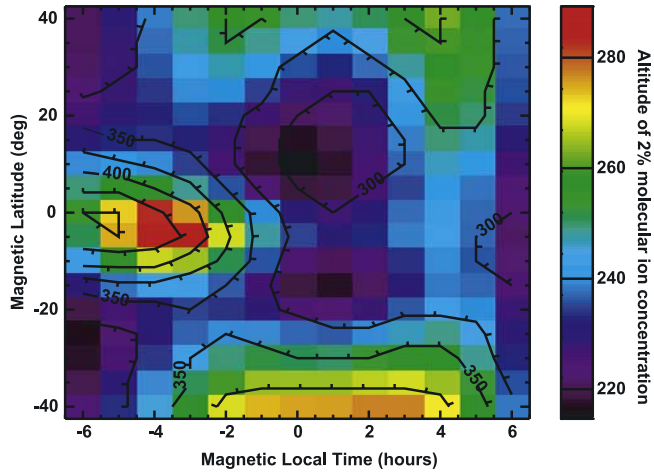

Figure 3. Altitude where the ratio of the molecular ion concentration to the atomic oxygen ion concentration is equal to 0.02 as a function of altitude and magnetic local time (see equation (8)). Neutral composition was calculated from MSIS90E [*Hedin*, 1991]. The labeled contours (with marks indicating decreasing values) show the altitude of the peak electron density given by IRI 2000 [*Bilitza*, 2001] at the given latitude and magnetic local time.

Combining equations (4) and (5) and assuming that O^+ is the dominant ion in this region we can write to first order

$$\eta_{135.6} = R_1[e]^2\left(1 - \frac{[O_2^+] + [NO^+] + [H^+]}{[O^+]}\right). \tag{6}$$

From this we see that the volume emission rate can be approximated as

$$\eta_{135.6} \cong R_1[e]^2 \tag{7}$$

in areas where the atomic oxygen ion concentration is significantly higher than the concentration of the other ions.

[11] For the purpose of the retrievals described below, the assumption of the dominance of O^+ is justified in the altitude region of interest, particularly at night. Near the top of the F region, the O^+ concentration will drop to the point where H^+ can become an important positively charged component of the ionosphere. A survey of the Atmospheric Explorer data (AE-E), however, shows that the density of H^+ rarely exceeds 10^4 cm^{-3} which is, as we shall see, well below the detection range of our retrievals. In short, if the O^+ density is small enough so that H^+ becomes significant, then the electron density is too small for us to detect. At lower altitudes, the molecular ions O_2^+ and NO^+ undergo rapid dissociative recombination and are quickly depleted after sunset. The reactions that control the nighttime concentrations of the molecular ions are shown in Table 1. Because of the rapid rate of dissociative recombination, the molecular ions can be considered to be in photochemical equilibrium. Using this assumption we can write the ratio of molecular ions to the atomic oxygen ions as

$$\frac{[O_2^+] + [NO^+]}{[O^+]} = \frac{1}{[e]}\left([O_2]\frac{R_5}{R_7} + [N_2]\frac{R_6}{R_8}\right). \tag{8}$$

Figure 3 shows the altitude at which the ratio on the right hand side of equation (8) reaches 0.02. At altitudes higher

than this, the ratio becomes very small. Also shown in this figure is the altitude of the peak electron density. From the figure we see that in most places the molecular ions only begin to become important below 250 km. Even in locations where the 0.02% contour is above 250 km, its location is significantly (100 km) below the electron density peak. Thus we are justified in using equation (7) to represent the emission rate for subsequent calculations.

3. Global Ultraviolet Imager (GUVI) Observations

[12] In its operational mode, the GUVI instrument functions as a linear array of 14 detectors, each obtaining a spectrum that is integrated on board to yield 5 "colors" [*Paxton et al.*, 1999]. This linear array subtends an 11.8° angle and is nominally oriented parallel to the orbital plane of the TIMED spacecraft. The array is scanned perpendicular to the plane of the orbit through an angle of 140° in a stepwise fashion every 15 s. The scan begins on the antisunward limb at a tangent altitude of about 525 km and moves downward onto the Earth and across to the sunward horizon. In this paper, we are only concerned with the first 32 steps of each scan, during which the GUVI field of view scans tangent altitudes in the approximate range of 110 to 525 km. In this way, the GUVI instrument scans the Earth's limb in roughly 2 s, repeating this measurement every 15 s. The geometry is such that about two thirds of the 11.8° field of view overlaps in subsequent scans. In summary, every 15 s, 14 nearly adjacent limb scans are obtained in five colors (of which we are interested here in the 135.6 nm color). The vertical separation between measurements in the scan varies from about 8 km (near a tangent altitude of 525 km) to about 20 km (near a tangent altitude of 110 km). For a detailed description of the GUVI instrument and its measurement geometry, see *Paxton et al.* [1999].

[13] The general equation of measurement for a given pixel i (corresponding to a unique combination of scan step and linear array element number) is

$$C_i = \int_{-\infty}^{0} dt \int_{0}^{\infty} d\lambda \int_{0}^{\pi} \int_{0}^{2\pi} A_i^*(t,\lambda,\theta,\phi) I(t,\lambda,\theta,\phi) \sin(\theta) d\phi d\theta, \quad (9)$$

where C_i are the counts in pixel i, A^*_i is the complete instrument function for i, I is the radiance (photons/(cm^2 s sr nm)), t is time, and λ is the wavelength. The spherical coordinates for this equation (s, θ, ϕ) are given in the spacecraft body system. In this spacecraft-centered system, the z axis points through the bottom of the spacecraft (where GUVI is mounted) and GUVI mirror is scanned in the (y, z) plane. During normal operations, the spacecraft z axis points downward and the y axis points along the normal to the orbital plane in the antisunward direction. The geometry of the observation is shown in Figure 4.

[14] In the altitude range of interest we can treat the atmosphere as optically thin for 135.6 nm photons. We can therefore write the intensity, $I(t, \lambda, \theta, \phi)$, in equation (9) as

$$I(t,\lambda,\theta,\phi) = f(\lambda) \int_{0}^{\infty} \eta_{135.6}(s,\theta,\phi) ds, \quad (10)$$

where $f(\lambda)$ is the spectral shape of the 135.6 nm emission.

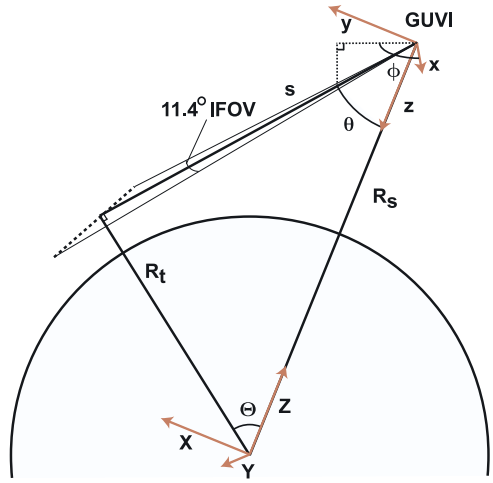

Figure 4. Diagram of the Global Ultraviolet Imager (GUVI) observation geometry. The Earth-centered coordinate system (X, Y, Z) and the Thermosphere Ionosphere Mesosphere Energetics and Dynamics mission (TIMED)-centered coordinate system (x, y, z) are defined in the text. Also shown are GUVI's 11.4° instantaneous field of view (IFOV) and the reference radii R_s, the radial distance to TIMED, and R_t, the radial distance to the satellite. The distance along the line of sight is labeled s.

[15] We represent the complete instrument response as the product of individual response functions:

$$A_i^*(t,\lambda,\theta,\phi) = A_i^t(t) A_i^\lambda(\lambda) A_i^\omega(\theta,\phi). \quad (11)$$

The time-dependent response function, $A_i^t(t)$, is rectangular over the integration interval of the instrument; that is, it is constant and nonzero over the integration time and zero everywhere else. Under the assumption that the intensity, I, changes little over the integration interval (32 ms), we can combine equations (9), (10), and (11) to yield

$$C_i = K_1 \int_{0}^{\pi} \int_{0}^{2\pi} \int_{0}^{\infty} A_i^\omega \eta_{135.6}(s,\theta,\phi) \sin(\theta) ds d\phi d\theta, \quad (12)$$

where K_1 is the calibration constant:

$$K_1 = \Delta t \int_{0}^{\infty} G(\lambda) A_i^\lambda(\lambda) f(\lambda) d\lambda, \quad (13)$$

where Δt is the integration time interval and $G(\lambda)$ contains the scaling factor converting intensity into counts. K_1 is determined from laboratory and on-orbit measurements of the instrument response.

[16] The measured brightness in Rayleighs for an individual pixel reported in the calibrated GUVI data (level 1B data available from the GUVI web site), B_i, is proportional to C_i. In Appendix A, we show that triple integral in equation (12) can be represented as a series of numerical quadratures. As a result, the measured brightness can be represented as a set of linear equations (see equation (A17)). The discrete linear form described in

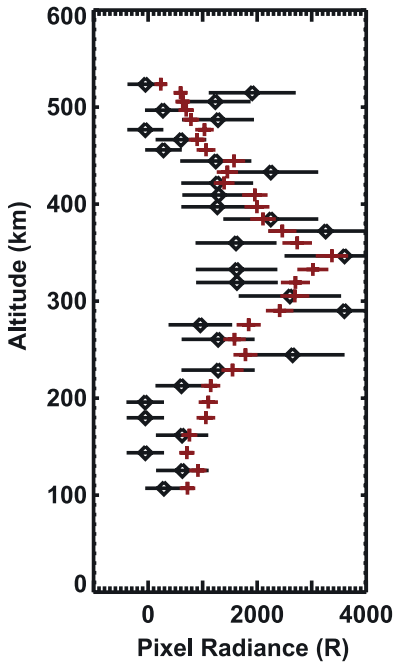

Figure 5. Profiles taken on 15 April 2002. The black diamonds with corresponding error bars show the data from the center along-track pixel. The red symbols with error bars show the 14-pixel average for the same integration period.

Appendix A will serve as a basis for the retrieval methods discussed below.

[17] Up to this point, we have assumed that the brightness, B_i, can be measured to a high degree of precision. However, the brightness on the limb at night corresponds to only a few counts per pixel in the brightest areas. There is, therefore, a large amount of statistical error in the individual measurements. Figure 5 shows a representative brightness profile for a single along-track pixel. Also presented in this diagram is the brightness for the same profile averaged over all 14 along-track pixels. Techniques for managing these rather large statistical errors are discussed below in the context of the retrieval algorithm.

4. Electron Density Retrievals

[18] Having described the observations and the basic equations required to interpret them, we now turn to the problem of inferring electron densities from them. From equations (7) and (A17) we see that the measured brightness in the 135.6 nm channel can be written in matrix form as

$$\mathbf{B} = \mathbf{W}\boldsymbol{\eta}([\mathbf{e}]), \tag{14}$$

where $\boldsymbol{\eta}([\mathbf{e}])$ is the volume emission rate to be retrieved at a fixed set of altitudes and $\mathbf{W}$ represents the geometric weights for each element along the lines of sight to which the measurements $\mathbf{B}$ correspond. The elements of $\mathbf{W}$ are

$$\frac{10^{-6}R_1}{4\pi}\left(w_{ij}^{(0)} + r w_{ij}^{(1)}\right), \tag{15}$$

where the $w_{ij}^{(k)}$ are geometric weights and r is the (small) roll angle perturbation of the spacecraft.The task at hand is to find an electron density profile that when substituted into equation (14) yields a brightness that is consistent with the measured brightness; that is, we minimize the quantity

$$\chi^2 = \frac{1}{N}(\mathbf{W}\boldsymbol{\eta} - \mathbf{B}_m)^T \mathbf{C}_m^{-1}(\mathbf{W}\boldsymbol{\eta} - \mathbf{B}_m), \tag{16}$$

where $\mathbf{B}_m$ is the measured brightness, $\mathbf{C}_m$ is the covariance matrix for the measurement and N is the number of measurements [see, e.g., *Rodgers*, 2000]. The covariance matrix is constructed by placing the squares of uncertainties on the diagonal and zeros everywhere else. At face value, this is a nonlinear least squares problem. In practice, we employ a two-step retrieval algorithm described below.

4.1. Refinement of the Equation of Measurement

[19] Before describing the retrieval method, we must refine the equation of measurement, equation (14), so that it can be used as the basis of a least squares retrieval. Standard least squares methods are best applied to data sets whose uncertainties are consistent with Gaussian statistics [see, e.g., *Menke*, 1989]. As is typical with instruments such as GUVI, the uncertainty in the measurements are most consistent with a Poisson distribution. As is shown in Figure 6, the Poisson distribution can be suitably approximated by a Gaussian distribution even at moderately low count rates ($\geq$10 or so). The GUVI measurements, however, have count rates that are below the range where this approximation is valid (see Figures 5 and 6). Because of the skew of the Poisson distribution at these count rates, we found that least squares techniques tended to seriously underestimate the retrieved electron densities.

[20] In order to account for this problem, we average over the 14 along-track pixels (see Figure 5). Doing so boosts the effective count rate into the range where Gaussian statistics can be used as a suitable approximation. The averaging is

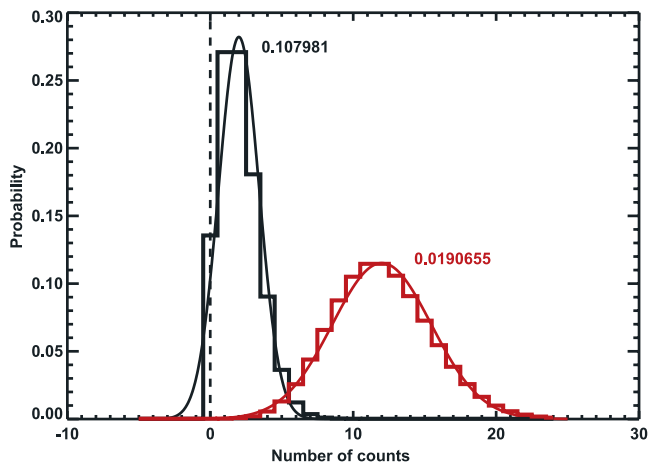

Figure 6. Poisson (histogram) and approximating Gaussian distributions (solid lines) for means of 2 (black) and 12 (red). The numbers beside the distribution peaks are the total integrated differences between the two distributions defined as $\sqrt{\int_{-\infty}^{\infty}\left(P_p(x) - P_g(x)\right)^2 dx}$, where $P_p(x)$ and $P_g(x)$ are the Poisson and Gaussian distribution functions, respectively.

implemented as follows. If the vector **B** in equation (14) is composed of all of the measurements in a single limb scan ($N = 32 \times 14 = 448$ pixels), we can define a linear averaging operator, $\mathbf{O}_a$ (with dimensions 32×448), which when applied to **B** results in an average brightness for each scan step, $\bar{\mathbf{B}}$. Using this operator we can rewrite equation (14) as

$$\bar{\mathbf{B}}([\mathbf{e}]) = \mathbf{O_a W}\eta([e]) = \mathbf{W_a}\boldsymbol{\eta}([e]). \tag{17}$$

The averaging must also be applied to equation (16), yielding

$$\chi_a^2 = \frac{1}{N_a}(\bar{\mathbf{B}}([\mathbf{e}]) - \bar{\mathbf{B}}_m)^T \mathbf{C}_{ma}^{-1}(\bar{\mathbf{B}}([\mathbf{e}]) - \bar{\mathbf{B}}_m), \tag{18}$$

where the following definitions have been made:

$$\begin{aligned} \bar{\mathbf{B}}_m &= \mathbf{O}_a\mathbf{B}_m \\ \mathbf{C}_{ma} &= \mathbf{O}_a\mathbf{C}_m\mathbf{O}_a^T \\ N_a &= N/14. \end{aligned} \tag{19}$$

Thus the refined problem, defined by equations (17) and (18), is formally identical to the original problem, defined by equations (14) and (16).

[21] The increased signal to noise realized by averaging the data allows us to treat the uncertainties in $\mathbf{B}_m$ as approximately Gaussian. This will permit us to use standard least squares techniques to solve the problem. In addition, the size of the problem is much smaller, so the numerical techniques applied will be significantly faster. The price paid for this simplification is minimal. Since the electron density profile is assumed to be spherically symmetric over the scale of the observations, averaging the 14 along-track pixels is equivalent to assuming there is no appreciable variation over about 3° in latitude.

4.2. Retrieval Method

[22] We begin the development of this method by noting that the electron density profile can be inferred directly from the volume emission rate via equation (7). If we can invert equation (A17) to determine the volume emission rate, then the electron density profile will follow easily.

[23] The linear least squares solution for $\boldsymbol{\eta}$ (equation (18)) is

$$\boldsymbol{\eta} = \left(\mathbf{W}_a^T\mathbf{C}_{ma}^{-1}\mathbf{W}\right)^{-1}\mathbf{W}_a^T\mathbf{C}_{ma}^{-1}\bar{\mathbf{B}}_m \tag{20}$$

[see, e.g., *Menke*, 1989]. Although equation (20) provides the solution that yields the smallest value of χ_a^2 in equation (18), there are two important problems with its application. First, as a result of marginal conditioning, the errors due to the uncertainties in $\bar{\mathbf{B}}_m$ are amplified in the solution for $\boldsymbol{\eta}$ [see, e.g., *Twomey*, 1977]. Second, in order to apply equation (7) to determine the electron density, we must take the square roots of the elements of $\boldsymbol{\eta}$. The solution must therefore be restricted to prohibit negative elements of $\boldsymbol{\eta}$. We must therefore modify the solution to yield more acceptable results.

[24] In order to ameliorate the conditioning problem, we add a linear smoothness constraint to equation (18); that is, we minimize the quantity

$$\chi_a^2 + \gamma\boldsymbol{\eta}^T\mathbf{H}\boldsymbol{\eta}. \tag{21}$$

The regularization matrix **H** is defined as

$$\mathbf{H} \equiv \mathbf{D}_2^T\mathbf{D}_2, \tag{22}$$

where $\mathbf{D}_2$ is the discrete implementation of the three-point second derivative operator. The tuning parameter γ will be discussed at length below. In using expression (21), we are jointly minimizing the prediction error (measured by χ_a^2) and the smoothness of the solution as measured by the quantity $\boldsymbol{\eta}^T\mathbf{H}\boldsymbol{\eta}$. Since the measure of smoothness is based on the second derivative of $\boldsymbol{\eta}$ with respect to altitude, solutions where the volume emission rate varies linearly (in a three-point group) are favored. The parameter γ determines how smooth the solution should be, with larger values of γ yielding smoother solutions. This method of imposing quadratic smoothness constraints is described in detail in the literature of remote sensing inverse theory [see, e.g., *Twomey*, 1977]. Of course, since we are no longer minimizing the prediction error alone, we run the risk of introducing systematic error into the solution. The appropriateness of using **H** as a smoothness constraint, the determination of a suitable value of γ and an analysis of the systematic error that these constraints introduce are all discussed in section 4.3.

[25] To prevent negative elements in the solution, we apply an iterative scheme proposed by *Menke* [1989]. The algorithm begins with an initial guess for the volume emission rate vector (in most cases we set all of the elements of this vector to zero). An initial solution vector, $\boldsymbol{\eta}_0$, is partitioned into two sets, 1) those elements that are zero, **S0**, and 2) those elements that are greater than zero, **S1**. At each stage of the iteration, k, the gradient of expression (21) is evaluated using the iteration from the previous step, $\boldsymbol{\eta}_{k-1}$. The element corresponding to the most negative gradient in **S0** (i.e., the element whose increase is most effective in decreasing the value of expression (21)) is moved to the set **S1**. A solution minimizing expression (21) is then calculated, $\boldsymbol{\eta}_k^0$, using only the points in **S1**. If this solution contains any negative elements, the difference vector,

$$\delta\boldsymbol{\eta} = \boldsymbol{\eta}_k^0 - \boldsymbol{\eta}_{k-1}, \tag{23}$$

is calculated. The solution is then adjusted to

$$\boldsymbol{\eta}_k = \boldsymbol{\eta}_{k-1} + \alpha\delta\boldsymbol{\eta}, \tag{24}$$

where α is as large as possible while eliminating negative elements in $\boldsymbol{\eta}_k$. This iteration proceeds until no elements can be moved from **S0** to **S1**; that is, the expression (21) cannot be made smaller by increasing one of the elements with a zero value. More details on this method can be found in the work of *Menke* [1989]. The net effect of this iterative method is to find a solution that minimizes expression (21) while eliminating the negative elements. We have found this

method to yield unique and reliable results when applied to the GUVI data as is demonstrated in the next section.

4.3. Tuning the Retrieval

[26] The proper adjustment of the tuning parameter, γ, in expression (21) is crucial to the success of our retrieval scheme. The value of γ determines how important the smoothness constraint is to the retrieval; that is, how much a priori information is introduced. When this parameter is too small, the retrievals tend to exhibit nonphysical oscillations and very large covariances that render the results of the retrievals useless. When γ is too large, the profiles become so smooth that they become inconsistent with the data from which they are derived. In this section, we address the proper selection of γ.

[27] Our selection of γ is based on the retrieval of simulated data sets. All of the data sets are based on a Chapman layer-like input electron density profile

$$[\hat{e}]_z = (1. \times 10^6) \exp\left[\frac{1}{2}\left(1 - \frac{z-364}{54} - e^{-\frac{z-364.}{54}}\right)\right]; \qquad (25)$$

that is, a Chapman function with a peak value of 1.0×10^6 cm^{-3}, a peak height of 364 km, and a topside scale height of 54 km. This represents a reasonable low-latitude nighttime profile. The electron density profile, $[\hat{e}]_z$, is used in equations (7), (A17), and (A15) to produce a simulated set of GUVI counts. The quadrature scheme used in equation (A17) uses 10 km grid as opposed to the operation retrieval grid of 20 km. We then produced 100 simulated GUVI data sets from the estimated counts, each with a different realization of Poisson noise consistent with the count rate. These 100 data sets are then used as input to the retrieval algorithm with values of γ ranging from 10^3 to 10^9. The resulting retrievals are then used to find a suitable value for γ.

[28] We use three metrics in our selection of γ. The first is χ_a^2, from equation (18), which measures the consistency of the data with the retrieval. The second metric, which we will refer to as ν, is the number of nonzero elements of the retrieved profile (i.e., the number of points in the final set **S1** in the algorithm described above). The third metric is defined as

$$g \equiv \sum_z \frac{\left([e]_z - [\hat{e}]_z\right)^2}{\sigma_z^2}, \qquad (26)$$

where $[e]_z$ are the elements of the retrieved profile vector and the σ_z are the retrieved uncertainties in the electron density profile calculated through standard error propagation methods [see, e.g., *Bevington and Robinson*, 1992]. The metric, g, measures the consistency of the retrieval with the input electron density profile. It is important to note that g depends on both the retrieved profile and its uncertainty. For small values of γ, the value of g can be quite small because of the large uncertainties associated with the retrieval even where the deviations from $[\hat{e}]_z$ are rather large.

[29] Figure 7 shows various relationships between the metrics described above for the simulated data sets. Figures 7a and 7b show the relationship of χ_a^2 and g with the number of nonzero points in each retrieval, ν. The figure shows that the retrievals that result in small values of ν are not likely to be successful as measured by either χ_a^2 or g. Conversely, all of the retrievals where $\nu \geq 13$ exhibit small values of both χ_a^2 and g. We can therefore consider as successful all retrievals where 13 or greater points are nonzero. This correlation between fitting success and ν allows us to use this statistic as a method for the selection of γ. Figure 7c shows the rate of fitting success (i.e., $\nu \geq 13$) as a function of γ. This curve exhibits a flat peak near 10^5. We select as optimal the largest value of γ that yields the peak success rate. Figure 7d shows the value of g for the successful retrievals as a function of γ, with the optimal γ marked. From the figure we see that at the selected value of γ, the value of g is indeed acceptable.

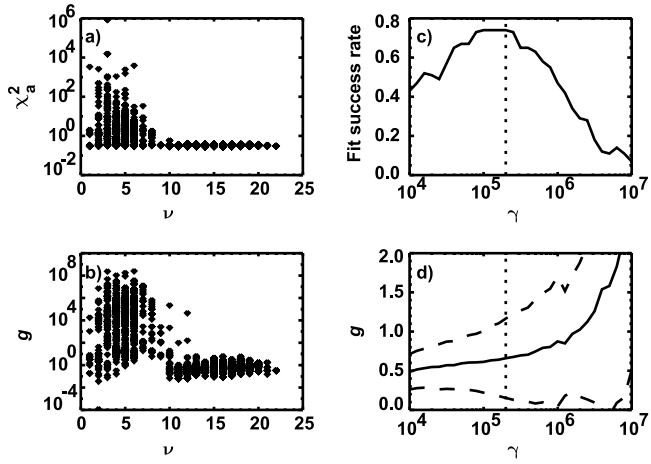

Figure 7. Plots of various elements of the constraints analysis for retrievals of a single GUVI radiance scan. (a) Scatterplot of χ_a^2 versus ν for each of the simulated retrievals. (b) Scatterplot of g versus ν for each of the simulated retrievals. (c) The fitting success (defined as the number of retrievals yielding $\nu \geq 13$ for a given value of γ) as a function of γ. The dashed line marks the position of the maximum γ that yields the largest fitting success. (d) The average value of g for the successful retrievals (solid line) and the one-standard-deviation envelope (dashed line) as a function of γ. Again, the dashed line marks the position of the maximum γ that yields the largest fitting success.

[30] Figure 8 shows a summary of the results of the successful retrievals where the selected γ is used. This figure shows both the errors introduced by fluctuations in the measurements and the systematic errors caused by the retrieval algorithms. The measurement uncertainties result in a spread of the values for the individual retrievals represented by the individual points in the figure. The systematic errors are shown by the difference between the diamonds (the average retrieved value) and the solid line (the input profile). Since we have used a large number of samples, the error in the mean, i.e., the position of the diamonds, is small relative to the scale on the figure. The average value of the retrieval (represented by the diamonds) is in generally good agreement with the input profile. Below 250 km and above 500 km the retrievals tend to overestimate the electron density. This is due to requirement that the electron density be nonnegative; that is, the nonnegativity restriction biases the retrieval to larger values, as values that in the absence of this restriction would be negative are

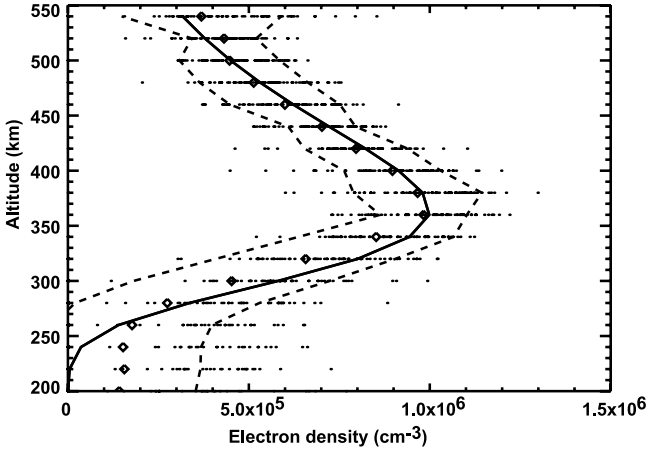

Figure 8. Retrieval and statistics for a single GUVI radiance scan using the maximum γ that yields the largest fitting success (see Figure 6). The solid line shows the input electron density profile, the diamonds show the average value of the retrieved profile, and the dashed lines show the one-standard-deviation error envelope. The dots show the results of the individual retrievals.

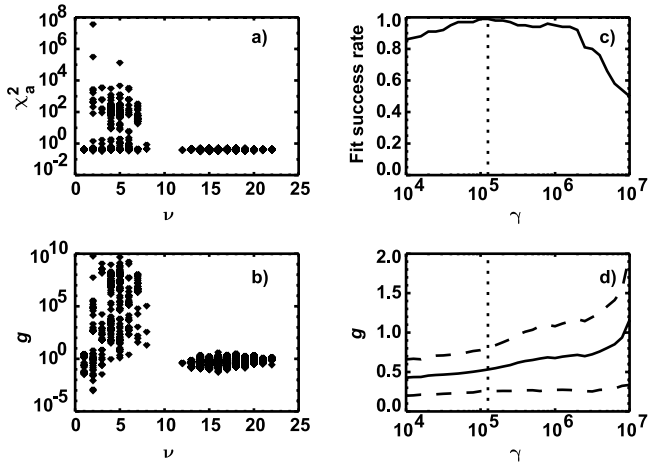

Figure 9. Plots corresponding to Figure 6 for nine scan averages appropriate for use with validation data sets.

artificially elevated to zero. The figure also shows an underestimate of a few percent in the retrievals between 275 km and the electron density peak. This is also a result of the nonnegativity constraint, in that underestimates in this area compensate for overestimates in the radiance from at lower altitudes. On balance, Figure 8 demonstrates that our retrieval scheme used with the selected value of γ yields a suitable electron density retrieval.

[31] In the next section, we will compare the results of the GUVI retrievals with incoherent scatter radar (ISR) data. In order to do so, we identified regions where GUVI and the various ISRs were observing similar volume elements. The observation and orbital geometry are such that the average time for which GUVI observed these volume elements with the ISRs was roughly 150 s. In order to more closely compare the GUVI and ISR data, we have averaged the GUVI measurements for the entire coincidence periods (by expanding the definition of the averaging operator $\mathbf{O}_a$ in equation (17)). Since averaging the data modifies the statistical characteristics of the retrievals, we repeated the above analysis for the selection of γ for 10 scan (i.e., 150 s) averages of the data. The results of this analysis are shown in Figures 9 and 10.

[32] From the figures it is immediately clear that the increased averaging and the corresponding increase in signal to noise has markedly improved the retrievals. Figure 9 shows a much higher success rate for the retrievals. Figures 9a and 9b now show a clear separation between the populations of successful and unsuccessful retrievals. Figure 9c shows that the success rate of the retrieval at the peak is nearly 100% and Figure 9d shows a narrower range of variation in the metric g. Figure 10 shows better agreement between the input and average retrieved profiles. The overestimates at each end of the altitude range are less pronounced, as well as the underestimates below the peak.

[33] In comparing Figures 8 and 10 we conclude that increasing the signal to noise ratio of the measurement not only yields a smaller covariance in the retrieval, but reduces systematic errors in the retrievals as well. This is primarily due to the nonnegativity constraint, though the fact that larger averaged count rates are more consistent with a Gaussian distribution may also contribute to this result. Thus in order to get full benefit from combining measurements from multiple scans (and therefore reducing the horizontal resolution) the data should be combined as part of the retrieval rather than averaging single scan retrievals after the fact; that is, the order of the processes of retrieval and averaging is important: One should first average and then retrieve. Careful consideration should be given to the required spatial resolution before using the retrieved data products. For studying high spatial resolution features in bright areas (for example in the equatorial anomalies), single scan retrievals are probably suitable. For more quantitative studies that include both bright and dim areas, spatial resolution should be sacrificed for the purpose of reducing biases in the retrievals.

5. Error Analysis

[34] There are several sources of error that must be considered when evaluating the fidelity of the retrieved

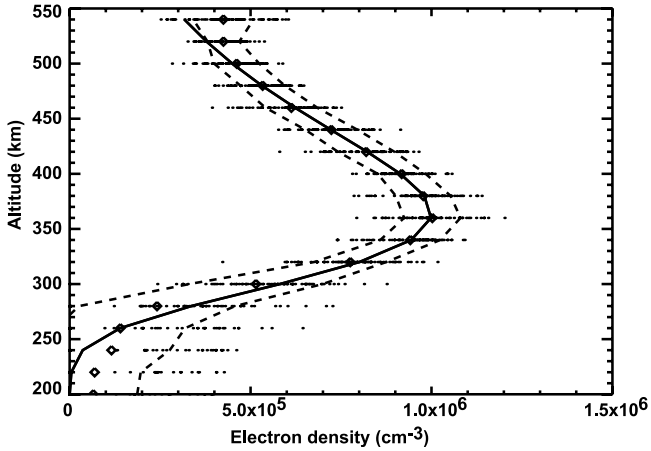

Figure 10. Plot corresponding to Figure 7 for 10 scan averages appropriate for use with validation data sets.

electron density profiles. The most obvious source of error is the statistical error in the retrieval resulting from the original uncertainty in the radiance measurement. The magnitude of this error is accurately estimated as part of the retrieval. Representative statistical errors are shown as the standard deviation envelope shown in Figures 8 and 10. In addition to the statistical uncertainty, there are several sources of systematic error that must be considered. Errors resulting from instrument calibration, a priori assumptions in the retrieval algorithm, and assumptions about the photochemistry will be described in this section in turn.

5.1. Instrument Calibration Errors

[35] There are three main areas of the GUVI instrument characterization that are important to the fidelity of the derived electron density profiles. First, there is the absolute calibration of the instrument. Second, there is the possibility of light from other spectral lines (most notably from 121.6 nm and 130.4 nm) contaminating the signal at 135.6 nm. Finally, there are the errors due to the uncertainty in the pointing of the instrument.

[36] The absolute calibration of the instrument is embodied in the quantity K_1 from equation (13). Changes in K_1 will result in the scaling of the matrix $\mathbf{W}$ in equation (14); that is, errors in the volume emission rate $\boldsymbol{\eta}$ will be proportional to errors in the absolute calibration. If we represent the error in the volume emission rate as a fraction difference, say Δ_a, we can write equation (7) with the error included as

$$\eta_{135.6}(1+\Delta_a) = R_1[e]^2. \tag{27}$$

From this equation it can be shown that to first order,

$$[e] = \sqrt{\frac{\eta_{135.6}}{R_1}}\left(1+\frac{1}{2}\Delta_a\right). \tag{28}$$

Thus the fractional error in the electron density will be half of the error in the absolute calibration. On the basis of both laboratory and in flight calibration experiments, the GUVI instrument absolute calibration error is less than 15%. Thus the corresponding error in the electron density will be less than 7.5%.

[37] The effects of errors due to light from other lines contaminating the 135.6 nm channel is somewhat more difficult to quantify. The main sources of contamination are from 121.6 nm and 130.4 nm, both of which are measured in other GUVI colors. The operational calibration algorithm (i.e., the algorithm that supplies us with the brightness) attempts to account for this contamination using the measurements from the other colors. From various calibration experiments it has been determined that the amount of contamination remaining from (or oversubtracted by) the operational algorithms for nighttime conditions is less than 1% of the brightness. Formally, the effect of color contamination on the volume emission rate depends on the inverse of equation (14). In practice, since both 121.6 nm and 130.4 nm vary slowly as a function on tangent altitude and any gross trends in tangent altitude dependence of the contamination from these lines are removed by the operational algorithm, we will assume that the errors in the volume emission rate scale approximately with the errors in the contamination subtraction, i.e., 1%. From analogy to equation (28), we see that the fraction error in the electron density due to this effect is roughly half of 1% or 0.5%, which is much smaller than the absolute calibration error.

[38] The primary effect of the pointing errors is the vertical displacement of the resulting electron density profile. Via in flight stellar calibrations, GUVI has been shown to have an approximate pointing accuracy of 0.05°. This corresponds to $\sim$2 km on the limb at 200 km tangent altitude and $\sim$1 km at 500 km tangent altitude. Thus altitude shifts in this amount may occur in the retrievals.

5.2. Retrieval Errors

[39] The a priori assumptions that were made in the construction of the retrieval algorithm can also contribute to the systematic error. There are four major sources of systematic retrieval errors that we will present here. First, we will examine the use of the continuous Gaussian distributions to represent what is more properly represented as discrete Poisson distributions. Next, we will examine the effects of the assumptions made during the tuning process described above. The assumption of the scale height for the exponential drop off above the tangent altitude of the highest measurement will then be discussed. Finally, the effects of horizontal smearing and the assumption of spherical symmetry will be described.

[40] As was described in section 4.1, the retrieval methods that we use depend on the assumption of Gaussian statistics for the measurement errors. The uncertainties in the GUVI data, however, are more properly represented by Poisson statistics, which are both quantized and skewed (particularly at small values). We have attempted to overcome this problem by averaging data from several measurements. This method has been reasonably successful, as is demonstrated by Figures 8 and 10. The retrieval errors shown in these figures (i.e., the difference between the solid lines and the diamonds) is due almost entirely to the approximations involved in the statistics of the uncertainties. For the cases presented in the figures, we see that the errors between 500 km and the electron density peak are quite small. Just below the peak, the errors in the single profile case (Figure 8) show errors of nearly 10%, though in the 10 profile average case this error is much smaller (see Figure 10). The figures also show that the retrieval behaves poorly well below the peak, i.e., for this case below 250 km, where the electron density is overestimated.

[41] In order to tune the retrieval algorithm (i.e., determine the appropriate value of γ), we assumed an electron density profile for the construction of a simulated data set. In doing so, we have made the implicit assumption that the profiles to which we apply the tuned algorithm are similar in character to this a priori profile. In order to test how sensitive the success of the algorithm is to this initial tuning, we have run an addition set of simulations. We simulated data using a variety of electron density layer heights and maximum magnitudes (with the appropriate random noise) and applied the tuned algorithm to it. The resulting metrics for these runs are shown in Figure 11. Figure 11 (left) shows the fitting success rate for the single profile (upper) and ten profile summed (lower) retrievals. Clearly there is a wide range of profiles that yield successful fits. Only profiles that have peaks well above 400 km or small peak magnitudes yield low success rates. From the figure we see that for single

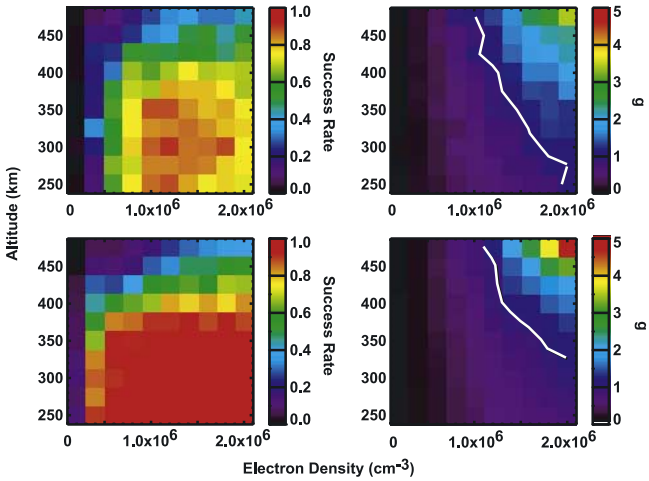

Figure 11. Effects of variability in electron density layer height and magnitude on the quality of the retrievals. (top) Success rate and the average g for single profile as a function of layer height and maximum magnitude for retrievals using the value of γ determined in the previous section. (bottom) Corresponding values for a 10-scan sum (as presented above). The white trace on the right-side plots shows the contour where the value of γ is equal to 1.

profile retrievals, it will be difficult to retrieve profiles with peak electron densities below 5×10^5. For the 10 scan retrievals however, profiles with peak magnitudes of 2×10^5 are likely to be successful. Figure 11 (right) shows the average metric g for these inversions. Again, we see a wide range of acceptable fits. The quality of the fits degrade at higher peak altitudes and magnitudes for both single and 10 profile retrievals. Thus for very high, large electron density layers a different tuning is appropriate. However, for most realistic profiles, the tuning parameters arrived at in the previous section can be applied with acceptable results.

[42] The retrieval also makes the assumption of an exponential drop off in volume emission rate (with a 50 km scale height) above the maximum altitude ($\sim$524 km). We have tested the sensitivity of the retrieval to the magnitude of this scale height by a similar process of simulation and retrieval. As is intuitively reasonable, systematic errors arise near the top of the retrieved electron density profile when various scale heights are used. However, for nearly all physically reasonable cases, the systematic error is negligible below 500 km. Thus we feel confident that our retrieval is suitably insensitive to the selection of the scale height for the drop off.

[43] As with most limb retrievals, our algorithms assume spherical symmetry. Violations of this symmetry can introduce errors into the resulting electron density profiles. The spatial scales for variation in electron density need to be compared to the scale sizes inherent in the retrieval. For an observation with a tangent altitude of 200 km, the tangent point is roughly 2400 km away from GUVI. At an altitude of 500 km, this distance shrinks to about 1300 km. For our retrievals to be representative of the actual electron density, this implies a scale size of about 1000 km over which spherical symmetry must hold. Fortunately, the features with the largest nighttime electron densities are the equatorial ionization anomalies, which are oriented in the direction of the magnetic equator. Since TIMED is moving in a roughly north-south direction near the equator, the GUVI line of sight is nearly parallel to the magnetic equator and the anomalies. Thus we are generally viewing in the direction of least horizontal variation. Also, since we have summed over the horizontal field of regard (and sometimes over several scans) we must also be concerned with the horizontal spatial scales perpendicular to the line of sight. For a 200 km tangent height, the 11.8° field of regard corresponds to about 500 km, while at 500 km this distance is reduced to about 270 km. Each 15 s scan moves the central tangent point a distance of about 100 km. Thus we should required spatial spherical symmetry scales to be a few hundred kilometers in this direction. Clearly, we are retrieving spatially smoothed quantities, with smoothing sizes of roughly 1000 km.

5.3. Errors in Photochemical Assumptions

[44] The retrievals are also sensitive to errors in the basic photochemical assumptions used in the construction of the techniques. This sensitivity enters through equation (7) and the simplifying assumptions made in its derivation. Clearly, the retrieval will be effected by the rate constant R_1 as appears explicitly in equation (7). Also, from the discussion in the previous section 2 we see that we have neglected the effects of mutual neutralization and the significant presence of positive ions other than O^+. These possible sources of systematic error will be discussed in turn.

[45] From equation (7) we see that errors in R_1 will result in proportional errors in the volume emission rate. Thus by analogy to equation (28), the resulting fractional error in electron density will be roughly half of the fractional error in R_1. We also note that *Meléndez-Alvira et al.* [1999] give the temperature-dependent value of this rate as

$$R_1 = 7.3 \times 10^{-13} \left(\frac{1160}{T_e}\right)^{1/2} \text{cm}^3\ \text{s}^{-1}, \qquad (29)$$

where T_e is the electron temperature in degrees Kelvin. Because R_1 is proportional to the square root of the electron temperature, the electron density will be proportional to $T_e^{1/4}$ and thus the fractional error in assuming a constant temperature profile will be about one fourth of the fractional change in temperature. Thus the effect of the temperature dependence on the retrieval is minor in the nighttime F region.

[46] In writing equation (7), we have neglected the effects of mutual neutralization (equations (2) and (3)) and significant concentrations of ions other than O^+ (equation (6)). We have shown these effects to be small over most of the range over which the retrievals are conducted. It is important to note that although the volume emission rate is modified by these factors, both of these effects are to some extent inversely proportional to the electron density. From equation (8) we see perturbations of the volume emission rate by concentrations of $[NO^+]$ and $[O_2^+]$ are explicitly inversely proportional to 1/[e]. The contribution to mutual neutralization of the electron density enters through its dependence on $[O^+]$. The overall effect of these dependencies is that these effects modify the electron density approximately linearly. For example, if $[NO^+]$ and $[O_2^+]$ represent 10% of the charge density at a given altitude,

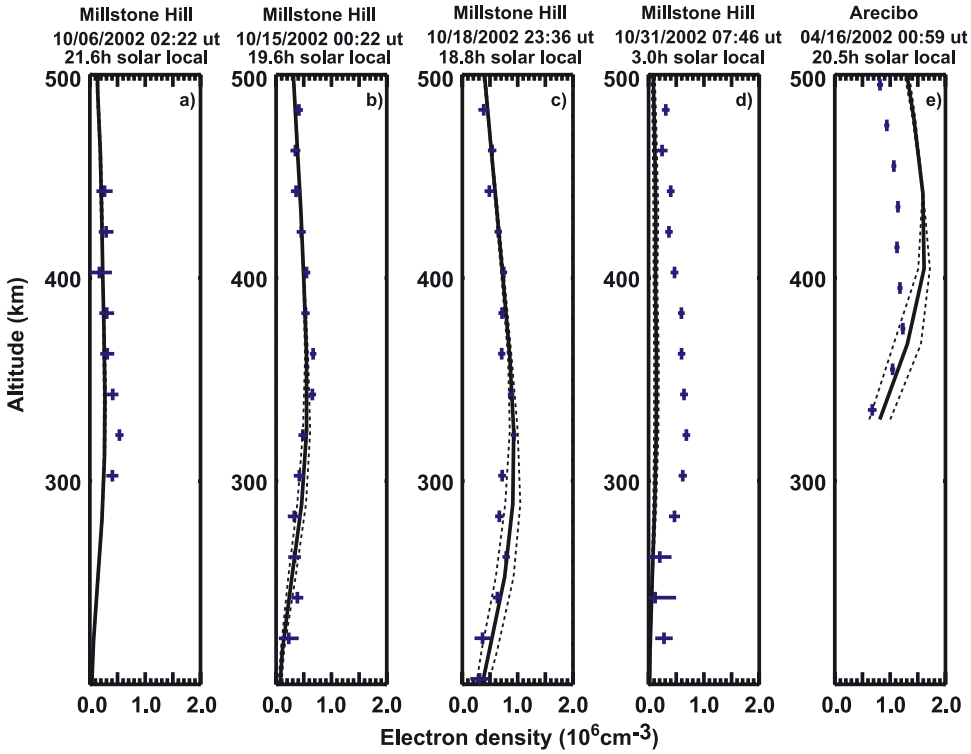

Figure 12. Comparison of electron densities inferred from GUVI data with those measured by the incoherent scatter radars (ISRs) at Millstone Hill and Arecibo. The solid lines show the 30 min averaged electron density profile measured by the ISR, with the broken lines marking one standard deviation around the mean. The 30 min window is centered around the time of coincidence with the GUVI observation. The blue symbols with error bars show the results of the GUVI retrievals.

we will underestimate the electron density by approximately 10%. All in all, however, we have shown in section 2 that there is a rather large range where these effects are not important, so the effect on most retrievals should be minimal. At both high and low altitudes, however, these effects may begin to become significant.

5.4. Summary of the Systematic Errors

[47] We have considered errors from statistical assumptions, instrument calibration, retrieval assumptions and photochemical uncertainties. The most significant source of error (in most cases) that we expect to find is the uncertainty in the absolute calibration of the instrument (approximately 7.5%). In addition, for single profile retrievals, the retrieval errors just below the electron density peak can be nearly 10% due to the statistical assumptions involved. Larger errors can occur for very high (>410 km) or very low (<250 km) electron density layers, where retrieval and photochemical errors begin to become important. Also, the retrieval may need to be retuned for very large electron densities to avoid significant errors. However, under most circumstances, we expect the systematic error in the retrieval to be around 7.5% for the multiprofile retrievals and down to the electron peak for the single profile retrievals.

6. Preliminary Validation

[48] In this section we will compare the retrievals described in the last section with nearly coincident measurements made by incoherent scatter radar (ISR) data. Note that the validation that we present here is preliminary; it is not a systematic evaluation of the accuracy of the retrievals. In order to conduct such a systematic validation, more ground truth data is required. What we present here are comparisons that demonstrate that our retrievals are indeed physically meaningful and can be considered quantitatively correct for a range of observation conditions pending a more complete validation effort.

[49] During 2002, we found several periods of coincidence of GUVI and ISR nighttime observations. Coincidence here is defined as when the GUVI tangent point at 300 km altitude passes within 500 km of the ISR. Most of the coincidences occurred over the Millstone Hill ISR while it was operating, though one was also identified above Arecibo while it was taking data. We took 30 min averages of ISR data, centered on the time of closest coincidence for comparison with the GUVI retrievals. As has been described in the previous section, the GUVI data during the coincidence period (in most cases 150 s) were combined to yield one retrieval per coincidence. Representative results of these comparisons are shown in Figure 12.

[50] We have included data from five of the coincidences in the figures. Figures 12a–12d show 4 of the 10 coincidences above Millstone Hill in 2002. These profiles are qualitatively similar to the other coincidences above Millstone Hill. Figure 12e shows the only available coincidence above Arecibo.

[51] Figure 12a shows a coincidence where the electron density over Millstone Hill is relatively small (less than 3×10^5 cm^{-3}). The agreement on the topside of the profile is good, however there is some disagreement near the peak of the profile. Figures 12a and 12b show substantially good agreement between the measurements where the electron concentrations are higher. The coincidence with Arecibo in Figure 12e, which exhibits very large electron densities with a fairly high altitude peak, shows agreement below 400 km but the GUVI data underestimates the electron density at higher altitudes. However, this coincidence occurred near a time where the F layer dropped very quickly over Arecibo (L. Goncharenko et al., Observations of the April 2002 geomagnetic storm by the global network of incoherent scatter radars, submitted to *Annals of Geophysics*, 2003). Thus the disagreement in the peak altitude may be an artifact of the rapid change of the ionosphere close to the measurements. Another important factor that may influence the quality of the retrieval is the large amount of electron density above the range of the GUVI measurement. On balance, for Figures 12a–12c and 12e we find reasonable agreement with some discrepancies that must be studied when additional data becomes available.

[52] Figure 12d, however, shows a fairly strong disagreement between the ISR and GUVI data sets. Profiles such as these are typical of the Millstone coincidences that were taken after local midnight. Inspection of the underlying GUVI data shows that the radiances received at GUVI are significantly larger than would be expected based on the ISR electron density profile. This leads us to conclude that in these cases, there is some source of 135.6 nm radiance other than O^+ recombination. Further investigation has revealed that during these times of elevated radiance, the magnetic field lines passing through the volumes of observation are illuminated by the sun in the southern hemisphere. We therefore conclude that conjugate photoelectrons produced in the southern hemisphere are transported along the magnetic field lines and are exciting atomic oxygen through photoelectron impact. The density of these photoelectrons relative to the ambient thermal electrons is small, they are therefore not measured by the ISR. Thus the GUVI retrievals should be used with care where there is a possibility of conjugate photoelectron contamination.

7. Summary and Conclusion

[53] We have presented here a method for deriving electron density profiles in the low/midlatitude nighttime ionosphere from the TIMED/GUVI instrument. We have described the underlying physical mechanism for the observation and presented the development of a retrieval technique for inference of electron density profiles. An error and constraints analysis has been provided for this technique that show it to reliably reproduce simulated data. The algorithms have been described here and applied to data taken in near coincidence with ground-based measurements. The agreement between the ground-based data and the electron density retrievals outlined here are good, though more work is required and more validation studies are necessary. Of particular interest is the postmidnight disagreement between the GUVI and Millstone Hill ISR data which suggests a source of 135.6 nm radiance which is not accounted for. Indeed a much more comprehensive validation should be undertaken using both ISR data for detailed profile comparisons and ionosonde data for statistical analysis.

[54] Nighttime electron density profiles from GUVI can provide important insight into the behavior of the ionosphere. Every TIMED orbit can provide a series of profiles covering the entire low and midlatitude ionosphere at a nearly constant local time. The precession of the TIMED orbital plane provides complete local time coverage in approximately 60 days. Thus this data set is well suited for producing seasonal characterizations of the ionosphere. Further, direct comparisons with independent measurement such as ISRs allow us to conduct detailed quantitative studies that may allow us to better understand the physical mechanisms that are important in the ionosphere.

Appendix A: Refining the Measurement Equation

[55] In this appendix we will show how the equation of measurement (equation (12)) can be represented in a form that is more conducive to inclusion in a numerical retrieval algorithm.

[56] The triple integral in equation (12) is carried out over all space in a spherical coordinate system. The volume emission rate, η, is primarily a function of altitude (or alternately Earth-centered radius R). It is convenient to rewrite the integral in equation (12) in terms of the Earth-centered coordinate system shown in Figure 4. In this system the Z axis points toward TIMED and the X axis is perpendicular to the orbital plane pointing away from the sun. Using this coordinate system, we can write

$$C_i = 2K_1 \int_0^{\pi} \int_0^{2\pi} \int_{R_t}^{\infty} A_i^{\omega} \eta_{135.6}(R) \frac{R^2}{s^2} \sin\Theta dR d\Phi d\Theta, \tag{A1}$$

where the TIMED-centered coordinates (s, θ, ϕ) are regarded as functions of the Earth-centered coordinates (R, Θ, Φ). Equation (A1) accounts for the fact that R is a double valued function of s that reaches a minimum at the tangent point radius R_t. In writing this equation, we assume that most of the emission takes place below the altitude of the spacecraft.

[57] The distance along the line of sight, s, can be expressed in Earth-centered spherical coordinates by applying the law of cosines:

$$s^2 = R^2 + R_s^2 - 2RR_s \cos\Theta, \tag{A2}$$

where R_s is the distance from the center of the Earth to the TIMED spacecraft.

[58] We now turn to the problem of expressing the body-centered coordinates (θ, ϕ) in terms of the Earth-centered coordinates. Figure 4 shows the nominal relationship between the two coordinate systems. This is the target orientation for the spacecraft's attitude system. In practice, there are always small variations between the nominal and the actual orientations. The variation between the nominal and actual attitude is characterized by a set of residual angles referred to as the roll, pitch and yaw angles, (r, p, y). These

angles are reported in regularly generated data products. The rotation matrix that connects the spacecraft and Earth-centered coordinate system can be written as

$$\mathbf{A} = \begin{vmatrix} -y & 1 & -p \\ 1 & y & r \\ r & -p & -1 \end{vmatrix}. \tag{A3}$$

This matrix is applied to vectors expressed in Earth-centered coordinates to express them in body-centered coordinates. Thus the line of sight unit vector, $\hat{\mathbf{s}}$, can be written as

$$\hat{\mathbf{s}} = \begin{vmatrix} \cos\phi \sin\theta \\ \sin\phi \sin\theta \\ \cos\theta \end{vmatrix} = \mathbf{A} \begin{vmatrix} \cos\Phi \sin\Theta \\ \sin\Phi \sin\Theta \\ \cos\Theta \end{vmatrix}. \tag{A4}$$

Using this equation and dropping terms that are second order in the small angles r, p and y, we can express the body-centered angles in the new coordinates as

$$\phi = \frac{\pi}{2} - \Phi + y + \alpha p \tag{A5}$$

and

$$\sin\theta = \frac{R \sin\Theta}{s}(1 - \alpha r), \tag{A6}$$

with

$$\alpha \equiv \frac{\cos\Theta - R_s/R}{\sin\Theta}. \tag{A7}$$

Equations (A2), (A5), and (A6) are the required relations that connect the two coordinate systems.

[59] We now turn to the spatial component of the instrument function $A_i^{\omega}(\theta, \phi)$. In the ϕ direction, the GUVI response is essentially a constant over a small angular interval and zero everywhere else. We therefore rewrite the spatial response as

$$A_i^{\omega}(\theta, \phi) = A_i^{\theta}(\theta) A_i^{\phi}(\theta, \phi), \tag{A8}$$

where the azimuthal response function is

$$A_i^{\phi}(\theta, \phi) = \begin{cases} 1 & \dfrac{|\phi - \phi_i|}{\sin\theta} < \dfrac{k_\phi}{2} \\ 0 & \text{otherwise} \end{cases}, \tag{A9}$$

where k_ϕ is a calibration constant specifying the azimuthal field of view of pixel i. Note that from equation (A5) we can write

$$\phi - \phi_i = -\Phi + \Phi_i, \tag{A10}$$

which allows us to represent the azimuthal dependence of the response function in the Earth-centered coordinates.

[60] Equation (A6) can be placed in a more convenient form for use with the remaining response function A_i^{θ}. If we define the quantity θ_0 by

$$\sin\theta_0 = \frac{R \sin\Theta}{s}, \tag{A11}$$

we can show that

$$\theta = \theta_0 + r\alpha \tan\theta_0, \tag{A12}$$

where θ_0 is the polar angle (in body coordinates) for the nominal orientation. This in turn can be used in the Taylor series expansion

$$A_i^{\theta}(\theta_0 + r\alpha \tan\theta_0) = A_i^{\theta}(\theta_0) + r\alpha \left.\frac{dA_i^{\theta}}{d\theta}\right|_{rpy=0} \cdot \tan\theta_0. \tag{A13}$$

Both A_i^{θ} and its derivative are known from the GUVI calibration. This expression allows us to express the instrument function in true orientation as a small perturbation of the instrument function in the nominal orientation. Note that only the roll angle, r, enters this expression to first order.

[61] Combining equations (A1), (A9), (A10), and (A13), we can write the brightness in Rayleighs for pixel i as

$$B_i = \int_{R_t}^{\infty} dR \psi_i^{(0)} \eta_{135.6} + r \int_{R_t}^{\infty} dR \psi_i^{(1)} \eta_{135.6}, \tag{A14}$$

where we have put

$$B_i = \frac{C_i}{2K_1 k_\phi} \tag{A15}$$

and have used the following definitions:

$$\begin{aligned} \psi_i^{(0)} &\equiv \int_0^{\pi} A_i^{\theta}(\theta_0) \frac{R}{s} d\Theta \\ \psi_i^{(1)} &\equiv \int_0^{\pi} \alpha \frac{R}{s} \left(\tan\theta_0 \left.\frac{dA_i^{\theta}}{d\theta}\right|_{rpy=0} - A_i^{\theta}(\theta_0) \right) d\Theta, \end{aligned} \tag{A16}$$

where we have put

$$B_i = \frac{C_i}{2K_1 k_\phi} \tag{A15}$$

and the calibration constant k_ϕ accounts for the field of view in the ϕ direction (i.e., the integral over d_ϕ in equation (A1)).The functions $\psi_i^{(k)}$ can be evaluated numerically (we employ a Gaussian quadrature scheme for this purpose). The integral in equation (A14) can be put in discrete form by means of Twomey type linear quadratures [*Twomey*, 1977] as

$$B_i = \sum_{j=1}^{N} \left[w_{ij}^{(0)} + r w_{ij}^{(1)} \right] \eta_{135.6}(R_j), \tag{A17}$$

with the following definitions:

$$
\begin{aligned}
w_{i1}^{(k)} &= \frac{R_2\mu_{i1}^{(0k)} - \mu_{i1}^{(1k)}}{R_2 - R_1}, \\
w_{iN}^{(k)} &= \frac{\mu_{iN-1}^{(1k)} - R_{N-1}\mu_{iN-1}^{(0k)}}{R_N - R_{N-1}}, \\
w_{ij}^{(k)} &= \frac{\mu_{ij-1}^{(1k)} - R_{j-1}\mu_{ij-1}^{(0k)}}{R_j - R_{j-1}} + \frac{R_{j+1}\mu_{ij}^{(0k)} - \mu_{ij}^{(1k)}}{R_{j+1} - R_j}, \\
\mu_{ij}^{(nk)} &= \int_{R_j}^{R_{j+1}} R^n \psi_i^{(k)} dR,
\end{aligned}
\tag{A18}
$$

where the radius (altitude) range has been represented as a discrete grid with N points R_j. In practice, we have altered the top quadrature weights, $w_{iN}^{(k)}$, to account for contributions to the integral in equation (A14) from above the uppermost quadrature point. For this purpose, we assume an exponential drop-off with a 50 km scale height above R_N. Equation (A17) is the form of the equation of measurement that will be used below to develop retrieval methods.

[62] From a practical point of view, it is important to note that the matrix elements $w_{ij}^{(k)}$ are the same for all of the GUVI observations. They are only a function of instrument calibration parameters, the nominal observing geometry and the quadrature grid, R_j. They need only be calculated once for all of the GUVI limb scans. The only geometric factor that influences equation (A17) is the roll angle, r.

[63] **Acknowledgments.** This work has been supported through the DMSP under task LBJ and NASA under task ICR at the Johns Hopkins University Applied Physics Laboratory. The Arecibo Observatory is operated by Cornell University under a cooperative agreement with the National Science Foundation. This work is part of the dissertation research of R. DeMajistre at the School of Computational Sciences at George Mason University, Fairfax, Virginia.

[64] Arthur Richmond thanks Rick J. Niciejewski for his assistance in evaluating this paper.

References

Bevington, P., and D. Robinson (1992), *Data Reduction and Error Analysis for the Physical Sciences*, 2nd ed., McGraw-Hill, New York.

Bilitza, D. (2001), International Reference Ionosphere 2000, *Radio Sci.*, *36*, 261–275.

Christensen, A. B., R. Walterschied, M. Ross, C. Meng, L. Paxton, D. Anderson, G. Crowley, S. Avery, R. Meier, and D. Strickland (1994), The Global Ultraviolet Imager (GUVI) for the NASA TIMED mission, in *Optical Spectroscopic Techniques and Instrumentation for Atmospheric and Space Research*, pp. 451–466, Soc. of Photo-Opt. Instrum. Eng., Bellingham, Wash.

Dymond, K. F., S. A. Budzien, S. E. Thonnard, R. P. McCoy, and R. J. Thomas (2001), Electron densities determined by the HIRAAS experiment and comparisons with ionosonde measurements, *Geophys. Res. Lett.*, *28*, 927–930.

Fehsenfeld, F. A., A. C. Schmeltekopf, D. C. Dunkin, and E. E. Ferguson (1969), Compilation of reaction rate constants measured in the ESSA flowing afterglow system to August 1969, technical report, Environ. Sci. Serv. Admin., Boulder, Colo.

Hedin, A. E. (1991), Extension of the MSIS thermosphere model into the middle and lower atmosphere, *J. Geophys. Res.*, *96*, 1159–1172.

Massey, H. S. (1969), *Electronic and Ionic Impact Phenomena*, vol. 2, Clarendon, Oxford, England.

Meier, R. R. (1991), Ultraviolet spectroscopy and remote sensing of the upper atmosphere, *Space Sci. Rev.*, *58*, 1–185.

Meléndez-Alvira, D. J., R. R. Meier, J. M. Picone, P. D. Feldman, and B. M. McLaughlin (1999), Analysis of the oxygen nightglow measured by the Hopkins Ultraviolet Telescope: Implications for ionospheric partial radiative recombination rate coefficients, *J. Geophys. Res.*, *104*, 14,901–14,913.

Menke, W. (1989), *Geophysical Data Analysis: Discrete Inverse Theory*, Academic, San Diego, Calif.

Olson, R. E., J. R. Peterson, and J. Moseley (1971), Oxygen ion-ion neutralization reaction as related to tropical ultraviolet nightglow, *J. Geophys. Res.*, *76*, 2516–2519.

Paxton, L. J., et al. (1999), Global Ultraviolet Imager (GUVI): Measuring composition and energy inputs for the NASA Thermosphere Ionosphere Mesosphere Energetics and Dynamics (TIMED) mission, *SPIE Opt. Spectrosc. Tech. Instrum. Atmos. Space Res., III*, *3756*, 265–276.

Roble, R. G., E. C. Ridley, and R. E. Dickinson (1987), On the global mean structure of the thermosphere, *J. Geophys. Res.*, *92*, 8745–8758.

Rodgers, C. (2000), *Inverse Methods for Atmospheric Sounding*, World Sci., River Edge, N. J.

Twomey, S. (1977), *Introduction to the Mathematics of Inversion in Remote Sensing and Indirect Measurements*, Elsevier Sci., New York.

Zeippen, C. J., M. J. Seaton, and D. C. Morton (1977), Some OI oscillator-strengths and interstellar abundance of oxygen, *Mon. Not. R. Astron. Soc.*, *181*, 527–540.

A. B. Christensen, The Aerospace Corporation, P.O. Box 92957, Los Angeles, CA 90098, USA. (andrew.b.christensen@aero.org)

R. DeMajistre, D. Morrison, L. J. Paxton, and J.-H. Yee, Applied Physics Laboratory, The Johns Hopkins University, 11100 Johns Hopkins Road, Laurel, MD 20723, USA. (robert.demajistre@jhuapl.edu; danny.morrison@jhuapl.edu; larry.paxton@jhuapl.edu; sam.yee@jhuapl.edu)

L. P. Goncharenko, Haystack Observatory, Massachusetts Institute of Technology, Route 40, Westford, MA 01886, USA. (lpg@haystack.mit.edu)